Effect of small inclination on binary convection in elongated rectangular cells

Isabel Mercader,[1,*] Oriol Batiste,[1,†] Arantxa Alonso,[1,‡] and Edgar Knobloch[2,§]
[1]*Departament de Física, Universitat Politècnica de Catalunya, 08034 Barcelona, Spain*
[2]*Department of Physics, University of California at Berkeley, Berkeley, California 94720, USA*

(Received 4 July 2018; published 26 February 2019)

We analyze the effect of a small inclination on the well-studied problem of two-dimensional binary fluid convection in a horizontally extended closed rectangular box with a negative separation ratio, heated from below. The horizontal component of gravity generates a shear flow that replaces the motionless conduction state when inclination is not present. This large-scale flow interacts with the convective currents resulting from the vertical component of gravity. For very small inclinations the primary bifurcation of this flow is a Hopf bifurcation that gives rise to chevrons and blinking states similar to those obtained with no inclination. For larger but still small inclinations this bifurcation disappears and is superseded by a fold bifurcation of the large-scale flow. The convecton branches, i.e., branches of spatially localized states consisting of counterrotating rolls, are strongly affected, with the snaking bifurcation diagram present in the noninclined system destroyed already at small inclinations. For slightly larger but still small inclinations we obtain small-amplitude localized states consisting of corotating rolls that evolve continuously when the primary large-scale flow is continued in the Rayleigh number. These localized states lie on a solution branch with very complex behavior strongly dependent on the values of the system parameters. In addition, several disconnected branches connecting solutions in the form of corotating rolls, counterrotating rolls, and mixed corotating and counterrotating states are also obtained.

DOI: 10.1103/PhysRevE.99.023113

I. INTRODUCTION

Binary fluid convection in a thin horizontal layer heated from below is a widely studied pattern-forming system that has contributed significantly to our understanding of generic features of out-of-equilibrium patterns undergoing symmetry-breaking bifurcations. In contrast to the pure fluid case, the dynamics near threshold can be much more complicated due to the extra degree of freedom associated with the concentration field. One experimentally relevant configuration for the study of pattern formation in binary mixtures, and the reference setup for our work, is that of a horizontal closed rectangular box heated from below. Experiments [1–4] and subsequent detailed numerical studies [5–9] showed that a variety of interesting spatially extended and spatially localized patterns arise in this configuration. However, convective systems in nature are often inclined with respect to gravity. Even when the cavity is intended to be placed horizontally, a very slight inclination may exist in a real physical situation. Tilting the cavity provides a simple and experimentally realizable way of introducing shear into the system via the generation of a large-scale circulatory flow. An interplay with the usual doubly diffusive convective mechanism is then expected to take place: The vertically sheared flow will differentially advect material properties across lateral fronts and the mixing and transport properties (momentum, heat, and solute) will be affected. Determining the extent to which the dynamics is modified when a convective layer is tilted is thus an important issue in many practical applications. The aim of this work is thus to explore and quantify the influence of a slight inclination on pattern formation in a closed rectangular cell containing a binary mixture.

Binary mixtures are characterized by the Soret effect, a cross-diffusion effect responsible for the diffusive separation of the lighter- and heavier-molecular-weight components when the mixture is placed in an imposed temperature gradient. The nondimensional parameter that quantifies the influence of this effect on the convective buoyancy force is the separation ratio S. In mixtures with $S < 0$, the type of mixtures we are interested in, the heavier component migrates towards the hotter region. If such a mixture is heated from below, the destabilizing temperature gradient sets up a competing stabilizing concentration distribution. The primary bifurcation of the conduction state is then a Hopf bifurcation [10], a fact that leads to rich dynamical behavior near the onset of convection.

The aforementioned small-scale experiments in laterally bounded rectangular containers [1–4] employed exquisitely controlled alignment and smoothness of the top and bottom plates and of their temperature. Corroborated by two-dimensional simulations in rectangular domains [5,6], these results revealed a complex sequence of transitions in the vicinity of the primary Hopf bifurcation involving three characteristic states of the system: chevrons (counterpropagating waves), blinking states (states dominated alternately by left- and right-traveling waves), and repeated transients (chevrons with growing amplitude that undergo repeated collapse to small-amplitude states). When larger

*maria.isabel.mercader@upc.edu
†oriol@fa.upc.edu
‡arantxa@fa.upc.edu
§knobloch@berkeley.edu

thermal stresses are applied to the layer, the system may evolve towards wall-attached confined patches of traveling rolls [11] or to steady convection, which can either fill the domain or form localized structures called convectons (bound states of fronts that connect the conduction state to the convection state). Convectons are organized in parameter space in a pair of intertwined snaking branches, consisting of even- and odd-parity states [7–9,12].

The effect of inclination on a convecting layer has been studied in numerous papers but almost entirely in one-component fluids. Early interest focused on the competition between longitudinal, transverse, and oblique rolls that arise from the primary bifurcation of the large-scale circulatory flow in extended layers. The corresponding experimental and numerical results are reviewed by Bodenschatz *et al.* [13]. More recent experimental [14,15] and numerical [16] studies of such extended layers show that a rich variety of spatiotemporal patterns may be realized when the inclination angle is varied. Other geometries have also been considered. Torres *et al.* [17] studied the transition from Rayleigh-Bénard convection to the heated-from-the-sides configuration in a closed parallelepiped. Convective patterns arising in a tilted cylinder at much larger rates of heating and for angles covering the Rayleigh-Bénard case are shown in [18]. These works cover a wide range of inclination angles and agree that for sufficiently small inclination angles the idealization of the physical system as being strictly horizontal works well and that the resulting pattern formation does not appear to be strongly influenced by very small inclination angles.

In contrast, previous numerical works on inclined binary mixture convection are scarce and mostly limited to studies of the onset of convection in two-dimensional or extended configurations. Numerical simulations of binary mixtures are much more costly, owing to the difference in relaxation times between the temperature and the concentration field arising from the sharp contrast between thermal and solutal diffusivities. Among relevant work on inclined two-dimensional binary fluid convection is an analytical and numerical study of natural binary fluid convection in an inclined shallow cavity with fixed flux boundary conditions on the temperature [19] and, more usefully for the present work, a related study of the onset of convection in an inclined infinite slot with fixed temperature boundary conditions [20]. More recently, experimental and numerical studies of convection in a slightly inclined disklike cylinder filled with an $S > 0$ mixture and subject to fixed temperature boundary conditions at the top and bottom [21,22] indicate that pattern formation is strongly affected even by small inclinations. Taken together, existing results on the tilted problem thus suggest that even very small inclinations produce substantial changes in the flow structure and result in new phenomena.

Bearing in mind the available results on binary mixtures, the aim of the present work is to analyze the effect of a slight tilt on the stability of the patterns arising in closed rectangular containers filled with an $S < 0$ mixture. We employ fixed temperature boundary conditions at the top and bottom and insulating sidewalls and wish to determine to what extent the breaking of symmetry that inclination implies affects the Hopf bifurcation of the conduction state and the emerging patterns (chevrons, blinking, and repeated transient states), as well as the snaking branches of localized steady convection. We perform two-dimensional simulations that provide a suitable model of convection in elongated parallelepipeds with a small transverse dimension. As shown in the experimental and numerical work of Kirchartz and Oertel on inclined pure fluid convection in confined cells of aspect ratios 10:4:1 and 4:2:1 [23], convection in these cavities sets in as transverse rolls for small inclinations that are well described by two-dimensional simulations, in contrast to what happens in laterally extended layers.

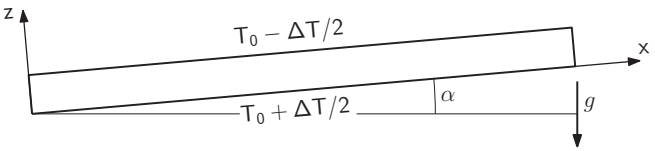

FIG. 1. Sketch of the domain geometry.

The organization of the paper is as follows. In Sec. II we formulate the equations, boundary conditions, and summarize the symmetries of the system. We also explain the numerical methods used. The main results are discussed in Sec. III. Specifically, in Sec. III A we summarize the main properties of the system with no inclination. Section III B then describes the large-scale base flow that arises when a small inclination is introduced and analyzes the properties of some of the multiple solutions obtained for inclination angles $\alpha = 0.01$ and 0.03. The corresponding results for $\alpha = 0.05$ are described in Sec. III C. The influence of the container aspect ratio and of the binary mixture parameters on the base flow is studied in Sec. III D, followed by a summary of the main results of the work in Sec. IV.

II. FORMULATION OF THE PROBLEM: EQUATIONS, SYMMETRIES, AND NUMERICAL METHODS

We consider two-dimensional Boussinesq binary fluid convection in a rectangular cell of height H and length L, inclined at a small angle α with respect to the horizontal. The cell is heated from below, ΔT being the temperature difference between the bottom and the top. We choose coordinates whose origin is located at the bottom left corner and oriented along the bottom wall (the x direction) and the sidewall (the z direction). In terms of these coordinates, the acceleration due to gravity takes the form

$$\mathbf{g} = -g\sin\alpha\,\hat{\mathbf{e}}_x - g\cos\alpha\,\hat{\mathbf{e}}_z.$$

A sketch of the domain geometry is shown in Fig. 1.

We split the temperature T and concentration of the heavier-molecular-weight component C_{heavy} into a linear profile in z and fluctuations Θ^* and Σ^* as follows,

$$\begin{aligned} T &= T_0 + \Delta T\left(\tfrac{1}{2} - z/H\right) + \Theta^*, \\ C_{\text{heavy}} &= C_0 - C_0(1-C_0)S_T\Delta T\left(\tfrac{1}{2} - z/H\right) + \Sigma^*, \end{aligned} \quad (1)$$

where T_0 and C_0 are the values of the temperature and concentration at midheight and S_T is the Soret coefficient, hereafter assumed to be negative so that the heavier component migrates towards the lower boundary in response to the applied temperature difference. Here H is the height of the cell. With

this decomposition the mass flux only depends on the gradient of Θ^* and Σ^*, the asterisk indicating unscaled quantities.

Scaling lengths with H, time with the vertical thermal diffusion time H^2/κ, κ being the thermal diffusivity, temperature with ΔT, and concentration with the induced concentration difference $-C_0(1-C_0)S_T\Delta T$, we obtain the dimensionless equations describing inclined binary fluid convection:

$$\begin{aligned}\mathbf{u}_t + (\mathbf{u}\cdot\boldsymbol{\nabla})\mathbf{u} &= -\boldsymbol{\nabla}P + \sigma\nabla^2\mathbf{u} + \mathrm{Ra}_z\sigma[(1+S)\Theta + S\eta]\hat{\mathbf{e}}_z \\ &\quad + \mathrm{Ra}_x\sigma[(1+S)\Theta + S\eta]\hat{\mathbf{e}}_x \\ &\quad - \mathrm{Ra}_x\sigma(1+S)(z-1/2)\hat{\mathbf{e}}_x, \\ \Theta_t + (\mathbf{u}\cdot\boldsymbol{\nabla})\Theta &= w + \nabla^2\Theta, \\ \eta_t + (\mathbf{u}\cdot\boldsymbol{\nabla})\eta &= -\nabla^2\Theta + \tau\nabla^2\eta, \end{aligned} \tag{2}$$

together with the incompressibility condition

$$\boldsymbol{\nabla}\cdot\mathbf{u} = 0. \tag{3}$$

Here $\mathbf{u} \equiv (u, w)$ denotes the nondimensional velocity field, P is the nondimensional mechanical pressure that includes parts of the buoyancy term that can be written as a gradient, Θ is the nondimensional temperature fluctuation, and $\eta \equiv \Sigma - \Theta$, where Σ represents the nondimensional concentration fluctuation. The variable η is defined such that its gradient is proportional to the dimensionless mass flux.

The system is thus specified by the inclination angle α and four dimensionless parameters: the Rayleigh number Ra that provides a dimensionless measure of the imposed temperature difference ΔT, the separation ratio S proportional to the Soret coefficient S_T that measures the concentration contribution to the buoyancy force due to cross diffusion, and the Prandtl and Lewis numbers σ and τ, respectively, in addition to the aspect ratio Γ of the rectangular cell. These parameters are defined as

$$\mathrm{Ra} = \frac{\gamma g \Delta T H^3}{\kappa\nu}, \quad S = C_0(1-C_0)\frac{\beta}{\gamma}S_T,$$
$$\sigma = \frac{\nu}{\kappa}, \quad \tau = \frac{D}{\kappa}, \quad \Gamma = \frac{L}{H},$$

where $\gamma > 0$ and $\beta > 0$ are the thermal and concentration expansion coefficients, D is the solute diffusivity, and ν is the kinematic viscosity. In these equations $\mathrm{Ra}_x = \mathrm{Ra}\sin\alpha$ and $\mathrm{Ra}_z = \mathrm{Ra}\cos\alpha$.

The resulting equations are to be solved subject to appropriate boundary conditions. We consider here the boundary conditions corresponding to impermeable no-slip boundaries with fixed imposed temperature at the top and bottom, and thermally insulating sidewalls. Thus

$$u = w = \Theta = \eta_z = 0 \quad \text{on } z = 0, 1 \tag{4}$$

and

$$u = w = \Theta_x = \eta_x = 0 \quad \text{on } x = 0, \Gamma. \tag{5}$$

As a measure of the heat transport by convection, we use the Nusselt number Nu, defined as the ratio of the heat flux through the top plate to that of the corresponding conduction solution and given by the expression

$$\mathrm{Nu} = 1 - \Gamma^{-1}\int_{x=0}^{x=\Gamma} \partial_z\Theta(z=1)dx.$$

We also evaluate, as an estimate of the strength of the convection, the dimensionless velocity norm E defined by

$$E = \Gamma^{-1}\int_{z=0}^{z=1}\int_{x=0}^{x=\Gamma} \mathbf{u}\cdot\mathbf{u}\,dx\,dz.$$

This quantity represents twice the kinetic energy per unit area of the system. In the following we refer to E for short as the mean kinetic energy.

As in earlier work [7–9], our computations are carried out mostly for the parameter values $\sigma = 7$, $\tau = 0.01$, and $S = -0.1$ and for aspect ratios around $\Gamma = 14$. Section III D is devoted to exploring the aspect ratio and binary mixture parameter dependence of some of our results. The physical parameter values we employ are appropriate for a number of experimental studies using water-ethanol mixtures, notably those performed by Kolodner [4]. However, in all prior experiments great effort has been made to level the experimental cell, thereby eliminating any convection arising from stray horizontal temperature or concentration gradients to the extent possible. In the present work we deliberately introduce such gradients by inclining the cell, albeit at a small angle α to the horizontal.

The above equations have an important symmetry: When $\alpha \neq 0$ the equations, together with the boundary conditions, are equivariant with respect to the symmetry group $Z_2 = \{I, R\}$, where I stands for the identity and R is a reflection with respect to the center of the cell. Specifically, the reflection R acts on the fields u, w, Θ, and η as follows:

$$\begin{aligned} R &: (x, z) \to (\Gamma - x, 1 - z), \\ (u, w, \Theta, \eta) &\to (-u, -w, -\Theta, -\eta). \end{aligned} \tag{6}$$

As a consequence, the equations admit solutions invariant under R as well as solutions that break the symmetry R. In the latter case the application of R to a nonsymmetric solution generates a distinct but symmetry-related solution. When $\alpha = 0$, i.e., the layer is horizontal, the symmetry group is enlarged and becomes the symmetry group D_2 generated by two separate reflections R_1 and R_2, the former corresponding to reflection in x alone and the latter to reflection in the layer midplane:

$$\begin{aligned} R_1 &: (x, z) \to (\Gamma - x, z), \\ (u, w, \Theta, \eta) &\to (-u, w, \Theta, \eta); \end{aligned} \tag{7}$$

$$\begin{aligned} R_2 &: (x, z) \to (x, 1 - z), \\ (u, w, \Theta, \eta) &\to (u, -w, -\Theta, -\eta). \end{aligned} \tag{8}$$

Notice that the reflection R corresponds to $R_1 \circ R_2$. The system of equations (2) and (3) and boundary conditions (4) and (5) has been solved numerically using the algorithm IPS described in [24], which can be summarized as follows. To integrate the equations in time, we use the second-order time-splitting method proposed in [25] combined with a pseudospectral method for spatial discretization that uses Chebyshev collocation in x and z. The Helmholtz equations obtained as a result of the splitting are solved using a diagonalization technique [26].

Steady solutions have been computed with Newton's method. We have used a first-order version of the time-

stepping code described above for the calculation of a Stokes preconditioner that allows a matrix-free inversion of the preconditioned Jacobian needed in each Newton iteration [27]. The corresponding linear system is solved by an iterative technique using the GMRES package [28]. The left-hand side of the preconditioned linear system (Jacobian acting on the correction) corresponds to one time step of the linearized equations and the right-hand side corresponds to performing one time step of the full nonlinear equations. In this way the Jacobian matrix is never constructed or stored [27]. The convergence criterion for the Newton method is 10^{-7}.

Once the steady states have been calculated by the method described above, their stability properties are determined by computing the eigenvalues and eigenvectors of the linearized problem using Arnoldi's method. The method calculates the dominant eigenvalues of the exponential of the Jacobian, which can be trivially related to the leading eigenvalues of the Jacobian, i.e., those with the largest real part. To this end, the algorithm for the time stepping of the linearized equations can be used since it in fact approximates the action of the exponential of the Jacobian on the solution at the previous time step. The eigenvalue computation itself has been implemented using the ARPACK package.

In the results reported in the present paper we have used a resolution that ensures variations of the Nusselt number or the mean kinetic energy smaller than 0.1%. We have used a grid of $n_x = 640$ and $n_z = 32$ points in the x and z directions, respectively, in a nondealiased code. For the time integration we have used the time step $\Delta t = 1 \times 10^{-3}$.

III. RESULTS

A. Noninclined system $\alpha = 0$

In previous work we have studied the problem of binary convection in a closed two-dimensional rectangular container heated from below and no inclination [5–9,12]. It is well established that the resulting system admits both spatially extended and spatially localized structures. The latter may be localized in the center of the domain or wall attached, either on one side or on both sides, thereby resembling a hole in an otherwise spatially extended state. Moreover, states in the form of bound states of two or more localized solutions, referred to as multipulse states [9], can also be present.

For the fluid parameters and the aspect ratio we consider in this paper ($\sigma = 7$, $\tau = 0.01$, and $\Gamma = 14$), the primary bifurcation of the $\alpha = 0$ conduction state is a Hopf bifurcation [6] that takes place at $\mathrm{Ra}_{\mathrm{Hopf}} = 1947.5$. In the vicinity of this bifurcation, computations reveal complex sequences of transitions among a state called a chevron state and two other states called blinking states and repeated transients as the aspect ratio or the applied Rayleigh number varies. The chevrons (or counterpropagating waves) consist of a pair of equal-amplitude waves, usually propagating outward from the cell center (i.e., left-traveling waves dominate in the left half of the domain, while right-traveling waves dominate in the right half), and these are the states that result from the primary Hopf bifurcation in domains that are not too large [5]. This primary bifurcation is subcritical, in agreement with the prediction for standing waves in a horizontally periodic system. The detailed properties and appearance of the time-dependent states depend crucially on the no-slip lateral boundary conditions which break the periodicity of the system in the x direction. Stable chevrons may be present in particular ranges of the aspect ratio Γ, but are most likely observed for values of Ra below its onset value. Stable small-amplitude blinking states set in when stable chevrons lose stability at a secondary Hopf bifurcation that produces oscillations in the amplitudes of the counterpropagating waves. Thus, the blinking states are alternately dominated by left- and right-traveling waves. A third type of state, the repeated transients, was observed by Kolodner in water-ethanol mixtures [4] very close to onset. These states consist of chevrons that grow exponentially from small amplitude without change of shape until they reach a critical amplitude at which they become unstable and collapse back to small amplitude. The repeated transients appear via a global bifurcation as the Rayleigh number Ra increases and may be the first nontrivial state that is seen. This state transitions into stable large-amplitude blinking states with a further increase in Ra. This transition has been identified as a tertiary Hopf bifurcation that eliminates the slowest frequency from the time trace and is typically hysteretic. With a further increase in the Rayleigh number, the system evolves either into wall-attached patches of traveling waves or towards steady convection, which can either fill the domain or form localized time-independent structures called convectons.

Convectons can be viewed as bound states of fronts that connect the conduction state to the convection state. Such states exist as a consequence of the pinning of the fronts to the finite-amplitude convection state and are present in a pinning region. There are two types of centered localized convectons: those invariant under R_1 (even convectons) and those invariant under $R = R_1 \circ R_2$ (odd convectons), organized in a pair of intertwined snaking branches in an (Ra, E) plot. As one proceeds up along each snaking branch, the localized states grow in length by nucleating new rolls on either side in such a way that the parity of the states is preserved. When the domain is almost filled the snaking must cease and the two snaking branches turn continuously into large-amplitude domain-filling states that resemble the mixed mode states computed with periodic boundary conditions. This continuous transition from spatially localized convectons to spatially extended structures is a consequence of the no-slip boundary conditions at the sides that eliminate the spatially periodic state [7]. It is important to note that each snaking branch in fact represents a pair of solutions related by the reflections R (even convectons) and R_1 (odd convectons) [9]. There are also branches of steady asymmetric states, called rung states, that connect the even and odd branches. These branches are born and die in parity-breaking bifurcations from the pure parity snaking branches. With periodic boundary conditions these states drift [9]. Holelike states and two-pulse states are also organized in snaking branches with reconnections between them that are also a consequence of the no-slip boundary conditions. Other snaking branches with connections between $n-1$ and n pulses are also present [9]. We note that for sufficiently negative values of the separation ratio like those used in this paper, the convecton branches do not connect to the base flow: All steady-state bifurcations of the base flow have been pushed off to infinity.

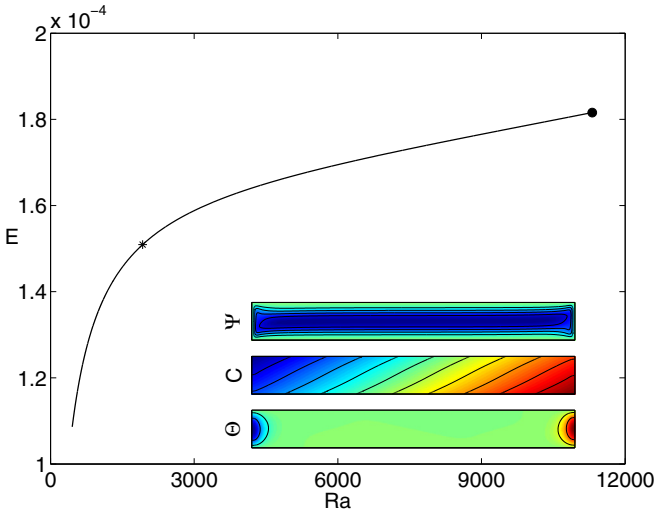

FIG. 2. Large-scale base flow when $\alpha = 0.03$. The curve shows the mean kinetic energy E of this flow as a function of Ra and the location of the Hopf bifurcation ($*$). The insets show contour plots corresponding to the stream function Ψ, concentration C, and temperature fluctuation Θ at Ra $= 11313$ (solid circle on the solution branch). In the colormap used here and throughout the paper, red corresponds to positive values of the field, blue to negative values, and green to zero. The parameters are $S = -0.1$, $\tau = 0.01$, $\sigma = 7$, and $\Gamma = 14$.

B. Very small inclinations $\alpha = 0.01$ and 0.03

In this section we present the results for inclinations $\alpha = 0.01$ and 0.03. When $\alpha \neq 0$ the character of the problem changes dramatically, largely because of the generation of a large-scale flow along the bottom wall with a return flow along the top wall. This flow is the unique solution at very low Ra and is referred to hereafter as the large-scale base flow (LSF). Physically, the appearance of this flow is a consequence of a nonzero component of the buoyancy force along the horizontal wall, while mathematically it is a consequence of the broken R_1 symmetry mentioned above.

In Fig. 2 we show the development of the LSF with increasing Ra for $\alpha = 0.03$ (in the following we measure α in radians). For the parameters used in this paper and for very small values of α, the large-scale flow that replaces the conduction state extends towards very large values of Ra. The insets in Fig. 2 show in succession the stream function Ψ ($u = -\Psi_z$ and $w = \Psi_x$), the total scaled concentration C [$C = -C_{\text{heavy}}/C_0(1 - C_0)S_T \Delta T$], and the temperature fluctuation Θ, computed at Ra $= 11\,313$ (solid circle in the bifurcation diagram; this circle does not represent the termination of the branch). The figure shows an R-symmetric solution with flow towards the right along the bottom boundary and to the left along the top boundary, as predicted by linear theory for an unbounded system [20]. In the present case the container is closed and the flow along the bottom boundary transports the higher concentration near the bottom boundary to the right, leading to a substantial increase in C at the right wall and a corresponding deficit near the left wall. The net effect of the base flow is to generate contours of constant concentration that have a constant positive slope, except very close to the sidewalls where the slope must be zero. This result is in qualitative agreement with linear stability theory [20], which predicts a slope proportional to $|S|/\tau$. Note that, despite the small value of the inclination α, the slope of the constant concentration contours is of order one. The existence of this base flow state is not at all surprising. However, it is unexpected that in order for the $\alpha \neq 0$ system to resemble the $\alpha = 0$ system the inclination α must be extraordinarily small, as we show below.

For these small inclinations, just as for $\alpha = 0$, the LSF destabilizes in a primary Hopf bifurcation that either respects or breaks its symmetry R and so gives rise to several time-dependent patterns. We begin by showing an example of the transient states that emerge as a result of this primary Hopf bifurcation when $\alpha = 0.03$. In Fig. 3 we show the time evolution of a small perturbation at a Rayleigh number slightly larger than the critical value for this bifurcation [$\varepsilon \equiv (\text{Ra} - \text{Ra}_c)/\text{Ra}_c = 7.6 \times 10^{-4}$]. Several patterns appear as transients before the final state is reached. First we see a growing chevron with a frequency close to the critical frequency $\omega_c = 6.04$ [Fig. 3(a)]. This state eventually saturates, but the saturated chevron state is not stable and evolves to a quasiperiodic pattern that does not correspond to the blinking state obtained when $\alpha = 0$. Instead of a pattern dominated alternately by left- and right-traveling waves, we first observe a modulation that corresponds to oscillations in the phase of the amplitude of the left- and right-traveling waves propagating outward from the center [Fig. 3(b)]. This pattern evolves quickly to a pattern resembling a standing wave confined to the left side of the container and a traveling wave on the right side of the container, with both regions separated by a very-small-amplitude central region (not shown). This pattern is in turn unstable and evolves to a chaotic blinking state in which we observe episodes dominated by either left- or right-traveling waves, or coexisting left- and right-traveling waves, or amplitude collapse [Fig. 3(c)]. These states are reminiscent of those studied in Ref. [29]. The time evolution of the mean kinetic energy and of the Nusselt number of this final state exhibits bursting behavior. When the Rayleigh number is decreased, this state persists to negative values of ε.

We now focus on steady localized solutions (centered convectons) that originate from the $\alpha = 0$ snaking diagram and consider the range of Ra for which such solutions exist. When $\alpha \neq 0$ the equations continue to admit solutions invariant under R (we retain the name odd-parity states for these states, as used in the $\alpha = 0$ case); Fig. 4(a) presents the snaking diagram for these states for $\alpha = 0.01$, i.e., the mean kinetic energy E as a function of the Rayleigh number Ra. Since the symmetry R_1 is broken, the odd-parity branch present for $\alpha = 0$ necessarily splits in two, leading to a pair of distinct snaking branches (blue and red), each consisting of R-symmetric states. Figure 4(a) also includes the snaking diagram for the odd-parity states when $\alpha = 0$ (black curve). States on the blue branch are characterized by a counterclockwise central roll, while states on the red branch have a clockwise central roll. Figure 4(b) shows an example of states on the blue and red branches at Ra $= 1973$ and Ra $= 1887$, labeled (2) and (1), respectively. Because of the pumping action associated with odd-parity states [7,12], the former state entrains heavier fluid from below on the right and lighter

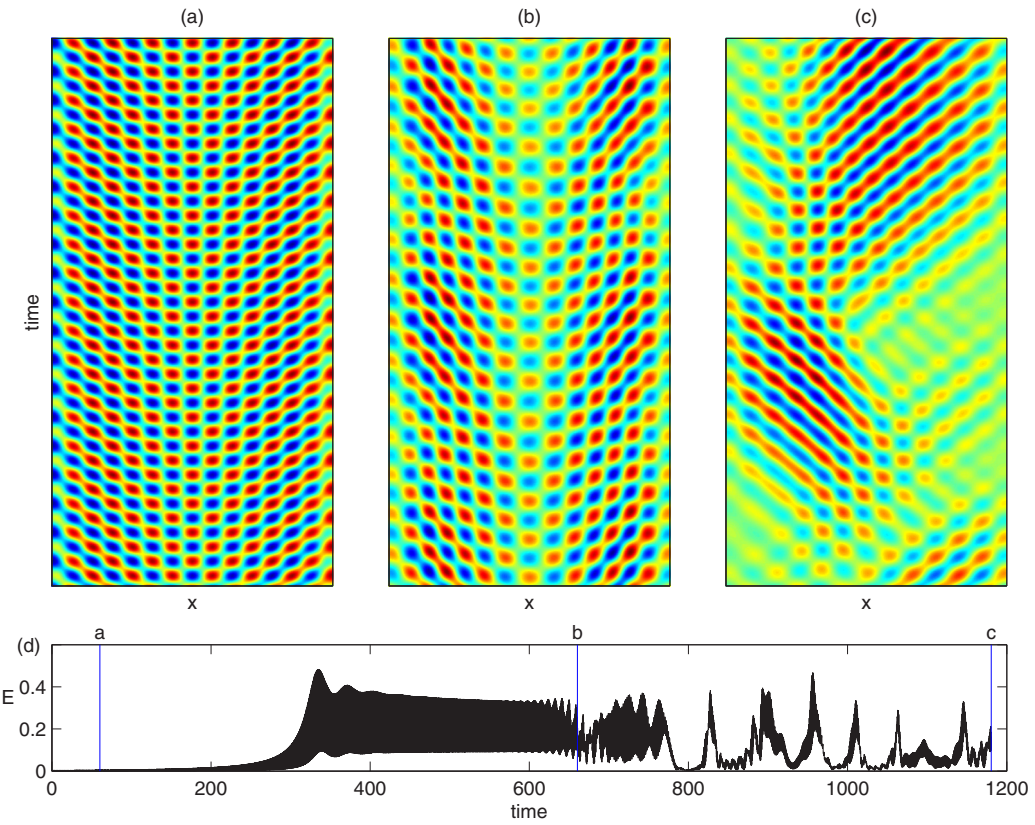

FIG. 3. Time evolution of a perturbation of the LSF near the primary Hopf bifurcation ($\mathrm{Ra}_c = 1923.54$) for a slightly supercritical Rayleigh number $\mathrm{Ra} = 1925$. (a)–(c) Space-time plots showing the evolution of Θ at midheight $z = 1/2$ with time increasing upward (each for 20 units of time) at the three instants indicated in the much longer time series shown in (d). (d) The mean kinetic energy E as a function of time t. The parameters are $\alpha = 0.03$, $S = -0.1$, $\tau = 0.01$, $\sigma = 7$, and $\Gamma = 14$.

fluid from top on the left. The result is a marked positive gradient in the contours of constant concentration C. Similar pumping takes place in the latter case, but because of the reversed circulation of the outer rolls the entrainment direction is reversed, resulting in a much starker left-right asymmetry in the concentration profile.

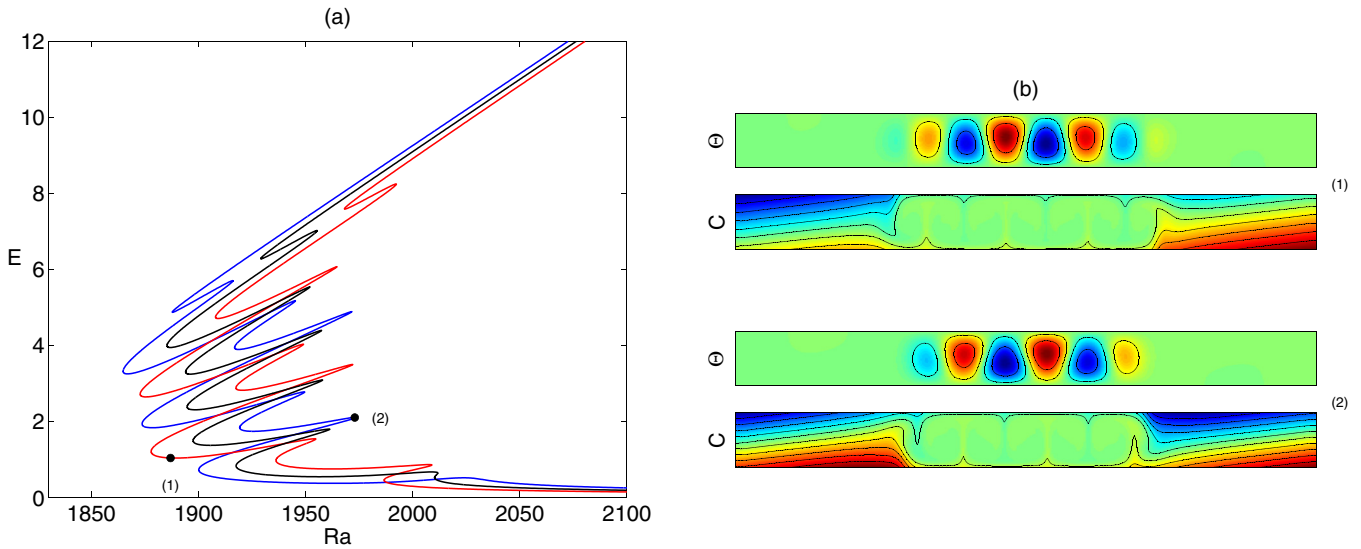

FIG. 4. (a) Snaking branches showing the splitting of the odd convecton branch for $\alpha = 0$ (black curve) when $\alpha = 0.01$ (blue and red curves). The states on the blue (red) curve correspond to states with a counterclockwise (clockwise) central roll. (b) Contour plots of constant temperature fluctuation Θ and concentration C for the counterclockwise (clockwise) central roll states indicated by solid circles on the corresponding branches. The parameters are $S = -0.1$, $\tau = 0.01$, $\sigma = 7$, and $\Gamma = 14$.

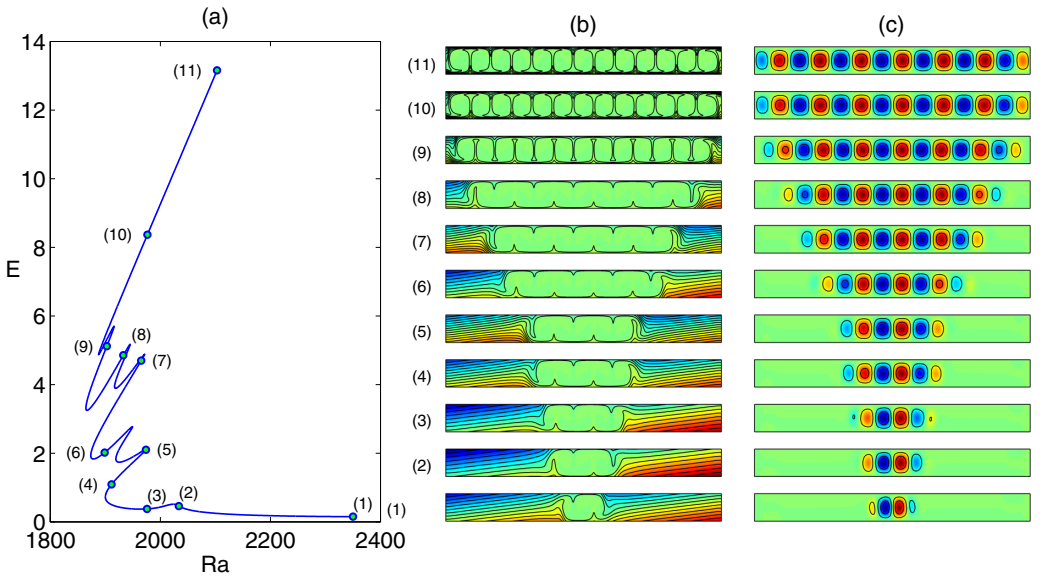

FIG. 5. (a) Snaking branch showing the mean kinetic energy E for solutions with a counterclockwise central roll (blue states) as a function of the Rayleigh number Ra when $\alpha = 0.01$, together with (b) the concentration C and (c) contours of the vertical velocity w at the locations indicated in (a). In both fields the same color bar is used for all the states. The parameters are $S = -0.1$, $\tau = 0.01$, $\sigma = 7$, and $\Gamma = 14$.

When $\alpha = 0$ the odd localized states undergo a sequence of back-and-forth oscillations within a well-defined snaking region, reflecting the addition of rolls on either side of the structure, until the domain is filled [black line in Fig. 4(a)]. The solution branch then turns towards higher values of Ra, growing the resulting domain-filling state in amplitude. This behavior is followed by both branches of odd convectons when α is small enough. Figure 5 shows sample states along the blue branch of such states corresponding to the locations indicated in Fig. 5(a) and summarizes the evolution of these states from a small number of rolls to larger-amplitude states with many more rolls where the convective structure turns into a domain-filling state. The figure shows that as one proceeds up the branch a state with counterclockwise rolls at the ends turns into one with clockwise rolls at the ends and back again, as the structure adds new rolls, one on each side. As a result, the pumping effect repeatedly changes direction as the structure grows. This is also the case along the red branch (not shown). Note that relative to the $\alpha = 0$ snaking branch, the new branches are obtained by shifting pairs of successive left-right folds in the $\alpha = 0$ diagram alternately inward and outward, an effect shown clearly in Fig. 5(a). Moreover, the pumping effect is more prominent when the number of rolls is small [Fig. 5(b)]: When the number is large a much larger fraction of the cell is homogenized and the effect of pumping correspondingly reduced.

In contrast to the odd solutions, the solutions originating from each pair of $\alpha = 0$ even convectons become asymmetric with respect to R_1 but continue to lie on a single branch in the bifurcation diagram because the symmetry R that relates them is not broken by the inclination. The asymmetric rung states, which are fourfold degenerate when $\alpha = 0$, also do not survive unchanged when $\alpha \neq 0$ and split into two pairs of asymmetric states which reconnect with the asymmetric states created from the $\alpha = 0$ even states. This reconnection leads to a breakup of the even states into a series of disconnected branches of asymmetric states. In Fig. 6 we show in green one of these disconnected pieces. It follows that the effects of $\alpha \neq 0$ are completely analogous to the effects of breaking the midplane reflection symmetry R_2 in the problem without inclination [30], or as described by Houghton and Knobloch [31], in the cubic-quintic Swift-Hohenberg equation, except that here the roles of the odd and even branches are reversed.

We consider now the results for a slightly larger value of the inclination, $\alpha = 0.03$. Figure 7 shows the corresponding results for the odd states (blue and red, as before) compared with the $\alpha = 0$ branch shown in black. Figure 8 shows details of the R-symmetric states on the blue branch. In comparison with the corresponding branch for $\alpha = 0.01$, we observe that at the bottom part of the branch the two consecutive inner saddle nodes have merged so that the solutions at successive saddle nodes on the left (locations 3 and 5) or on the right (locations 4 and 6) now differ in adding two new rolls on either side of the convecton structure as one proceeds towards larger energy E. In the upper part of the snaking structure, the complex behavior near location 8 is a consequence of the fact that at this location the remaining domain width is larger than that required for the insertion of a weaker cell near the no-slip boundary. Consequently, the structure must first adjust its internal wavelength before the insertion of the boundary rolls succeeds and the state becomes a true domain-filling state. This is the physics behind the complex structure of the blue branch near the transition to the domain-filling state.

Finally, it is also worth mentioning the behavior of the lower part of the snaking branches when α is small and the Rayleigh number Ra is increased: In contrast to the $\alpha = 0$ case, the red and blue branches do not extend to infinity. Instead, both turn around in a fold at large Ra and reenter the snaking region. For example, the red branch in Fig. 4 turns around at Ra $\sim$ 8200, where a single-pulse state (a clockwise roll in the center of the domain with a counterclockwise roll on both sides) starts to split and turns into a two-pulse state.

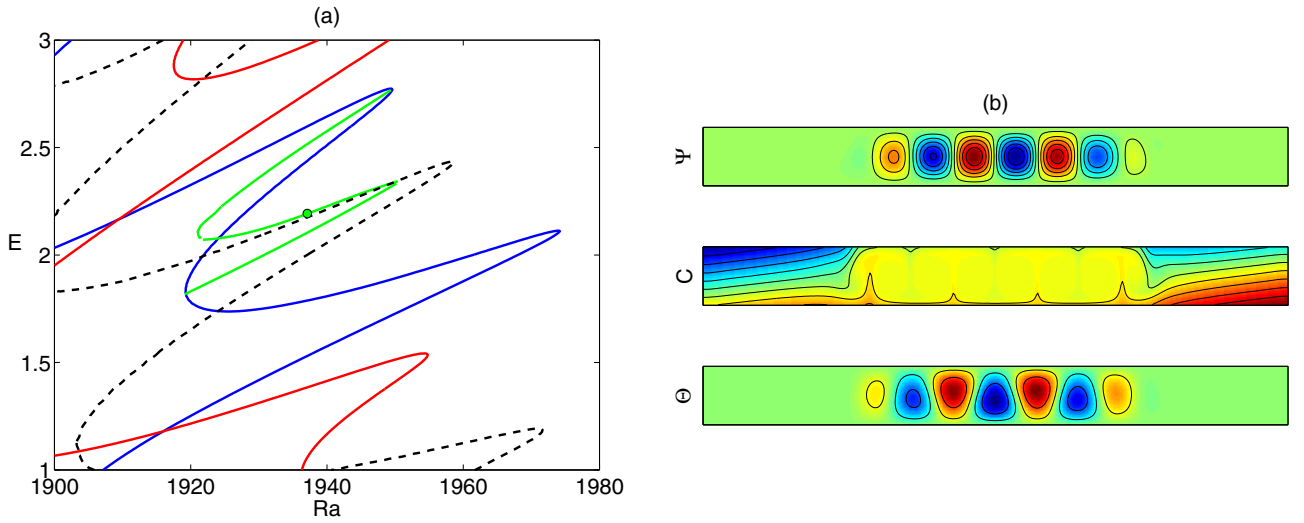

FIG. 6. (a) Mean kinetic energy E of asymmetric states (green curve) as a function of the Rayleigh number Ra when $\alpha = 0.01$, superposed on the corresponding snaking branches of odd states from Fig. 4 (blue and red solid lines); the dashed line indicates the snaking even-parity states when $\alpha = 0$. (b) Stream function Ψ and contours of constant concentration C and temperature fluctuation Θ of an asymmetric solution at the location indicated in (a) by the open circle. The parameters are $S = -0.1$, $\tau = 0.01$, $\sigma = 7$, and $\Gamma = 14$.

This state then undergoes two pairs of additional folds, one at Ra $\sim$ 6020 and 7180 and one at Ra $\sim$ 2420 and 2720, before undergoing two-pulse snaking within the same snaking region as the single pulse states, much as occurs in the $\alpha = 0$ case when the lateral boundary conditions are nonperiodic [9], as is the case here. These two-pulse states are omitted from Fig. 4. The states on the blue branch behave broadly similarly, although the transition to the two-pulse states now occurs at slightly larger α. Prior to the transition (i.e., at smaller α) one finds that the central roll splits at larger Ra into three much smaller and vertically staggered corotating rolls before the solution branch turns around towards smaller Ra. These states are also not shown here because the behavior of the lower part of the snaking branches is in fact extremely sensitive to the precise value of the inclination α (and the type of branch: clockwise or counterclockwise central roll) and remains to be fully elucidated. The relevant fluid mechanical reasons for this sensitivity to the inclination are discussed further in Sec. IV, with the relevant mathematical considerations likely resembling those in Ref. [32]. In any case, we see that for these very small values of the inclination α the localized states are not connected to the LSF branch which continues monotonically to large values of the Rayleigh number Ra (Fig. 2).

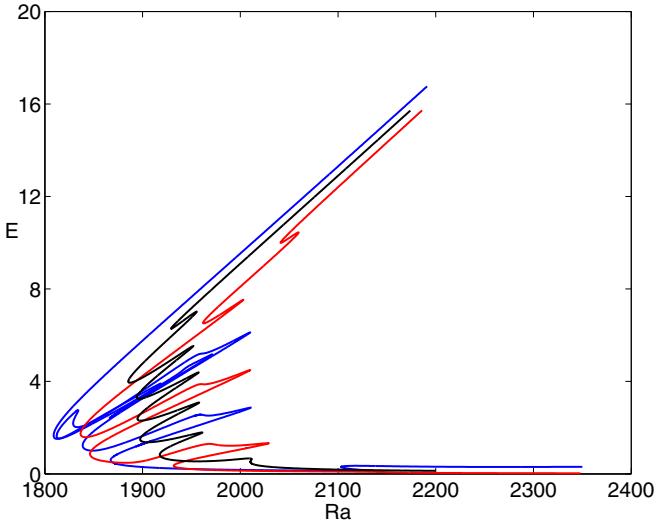

FIG. 7. Snaking branches showing the splitting of the odd convecton branch for $\alpha = 0$ (black curve) when $\alpha = 0.03$ (blue and red curves). The states on the blue (red) curve correspond to states with a counterclockwise (clockwise) central roll. The parameters are $S = -0.1$, $\tau = 0.01$, $\sigma = 7$, and $\Gamma = 14$.

C. Small inclination $\alpha = 0.05$

We now present the results obtained for a slightly larger inclination $\alpha = 0.05$. We aim to find out how increasing the strength of the large-scale flow affects the base flow branch and the branches of localized states obtained earlier for smaller inclinations. As we will see, this relatively small change in α changes completely the arrangement of the solution branches.

We explore first the evolution of the large-scale flow. Figure 9 shows that when the Rayleigh number exceeds a critical value of order Ra $\sim$ 1050 the base flow ceases to be featureless and starts to develop a localized roll in the center of the domain (location 1). The formation of this roll is associated with the presence of a fold at Ra $\sim$ 1050. When the resulting subcritical branch is followed to lower Ra and then past the next fold on the left this central roll becomes strongly localized and a new state results (location 2), characterized by a single counterclockwise roll embedded in a much-lower-amplitude background. Although it may seem from an inspection of the stream-function contour plots that increased inclination suppresses the base flow completely, this is not the case. The shear horizontal velocity is still present, but its amplitude is much lower than that of the velocity field

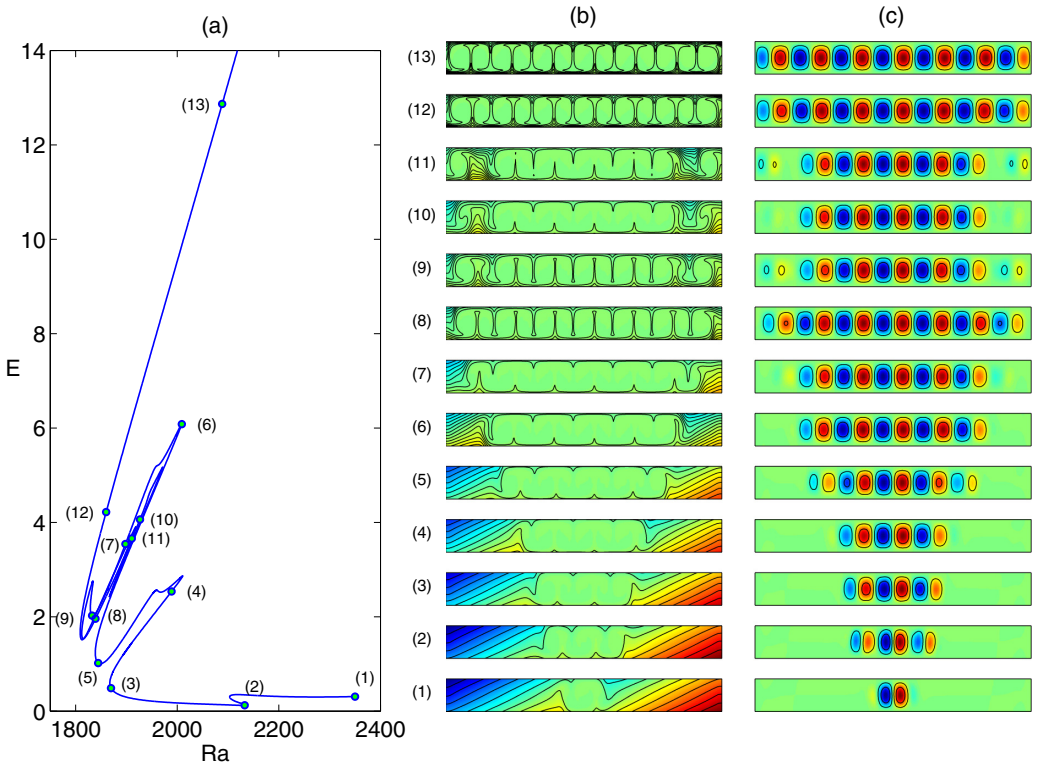

FIG. 8. (a) Snaking branch showing the mean kinetic energy E for solutions with a counterclockwise central roll (blue states) as a function of the Rayleigh number Ra when $\alpha = 0.03$, together with (b) the concentration C and (c) contours of the vertical velocity w at the locations indicated in (a). In both fields the same color bar is used for all the states. The parameters are $S = -0.1$, $\tau = 0.01$, $\sigma = 7$, and $\Gamma = 14$.

within the localized rolls. As a result, the colormap used to plot the figures makes the background look, misleadingly, quiescent. The different scale that is used for the stream-function representation helps to visualize the flow, while the velocity amplitude can be inferred from the mean kinetic energy plot. As one follows the branch to larger amplitude

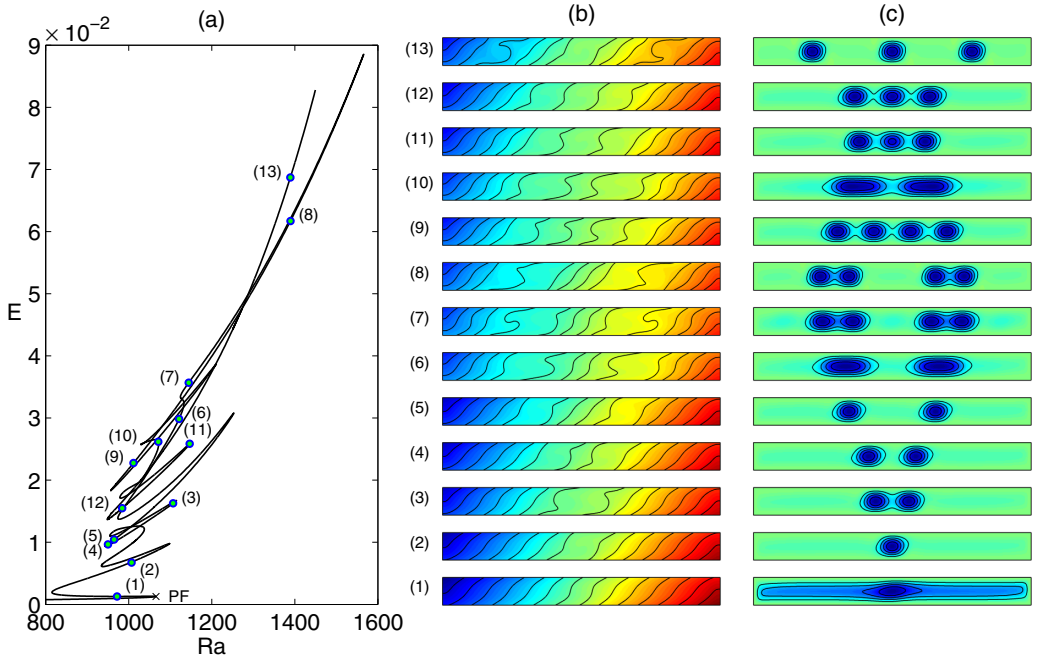

FIG. 9. (a) Complex curve showing the mean kinetic energy E for solutions obtained by numerical continuation of the large-scale flow with the Rayleigh number Ra when $\alpha = 0.05$. The letters PF indicate the primary fold. (b) Concentration C and (c) contours of the stream function Ψ at the locations indicated in (a). In the concentration contours the same color bar is used for all states, while a variable scale is used for the stream-function representation to ease visualization. The parameters are $S = -0.1$, $\tau = 0.01$, $\sigma = 7$, and $\Gamma = 14$.

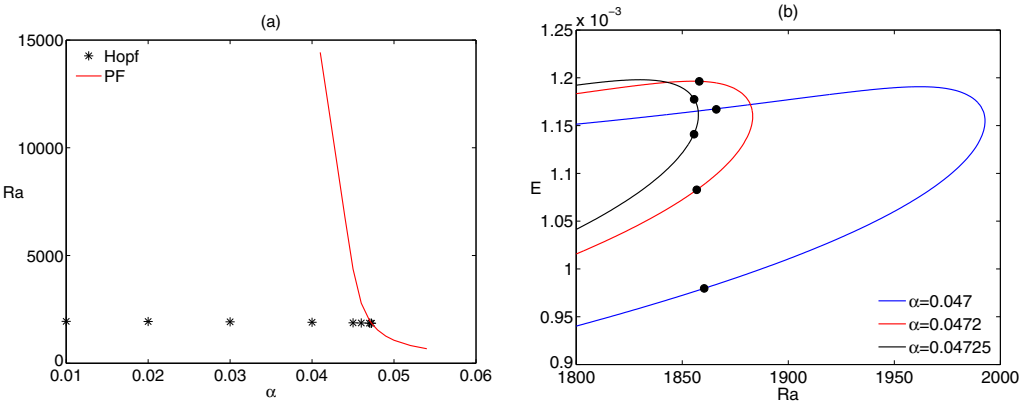

FIG. 10. (a) Critical Rayleigh number Ra as a function of the inclination α corresponding to the primary Hopf bifurcation of the LSF ($*$) and to the primary fold (red curve). (b) Mean kinetic energy E as a function of the Rayleigh number for different inclinations near the α value where the Hopf bifurcation disappears. Solid circles indicate the upper and lower Hopf bifurcations. The parameters are $S = -0.1$, $\tau = 0.01$, $\sigma = 7$, and $\Gamma = 14$.

the number of rolls gradually increases. What is of interest, however, is that the next state that is encountered (location 3) consists of two rolls, both of which rotate in the counterclockwise sense. The tendency to generate corotating rolls with increasing Rayleigh number is of course well known for doubly diffusive convection in a vertical slot [33,34], but what is of particular interest in the present case is that this already occurs for the very small inclinations used here. This process is a consequence of the interaction between the base flow and the rolls, the flow strengthening rolls that rotate in the same sense as the base flow but weakening those that rotate counter to it. As one follows the branch farther upward these corotating rolls gradually drift apart before expanding laterally (location 6) and then splitting into two pairs of corotating rolls. These drift towards each other as one follows the branch yet farther, forming a four-roll localized state (location 9). A similar sequence of transitions subsequently generates a state consisting of three equidistant corotating but isolated rolls (location 13). We have continued this solution branch much farther (not shown) and have not reached a domain-filling state. Following the solution branch from location 13, one finds there are many subsequent sharp folds, corresponding to lateral displacements of the three rolls, which increase and decrease their kinetic energy as the Rayleigh number varies, while the number of rolls remains constant (there are always three corotating rolls). The highest Ra value reached along this path was Ra $\sim$ 2285, with a mean kinetic energy $E \sim 1.29$, far beyond the limits of Fig. 9(a).

In the evolution of the large-scale flow curve we have just described, the location on the curve of the first fold on the right (Ra $\sim$ 1050) is evidently going to play a key role, since it marks the location where the large-scale base flow is overcome for the first time by vertical motions due to vertical temperature gradients as opposed to horizontal temperature gradients. Hereafter we refer to this fold as the primary fold.

Since the primary fold at $\alpha = 0.05$ occurs at quite low values of Ra, it is necessary to examine its competition with the primary Hopf bifurcation of the LSF as α increases from $\alpha = 0$. In Fig. 10(a) we indicate, as a function of the inclination, the critical Rayleigh numbers corresponding to the primary Hopf bifurcation of the LSF and to the primary fold. Whereas the Hopf bifurcation hardly varies with α, the values of Ra at which the primary fold takes place increase substantially as the inclination decreases, i.e., the first appearance of significant vertical motions is delayed to larger and larger values of Ra. These vertical motions arise in different locations within the domain depending on the inclination. We find that for inclinations larger than $\alpha = 0.045$ a localized roll develops in the center of the domain as in the $\alpha = 0.05$ case. For slightly smaller inclinations, beyond the fold bifurcation, the vertical motions

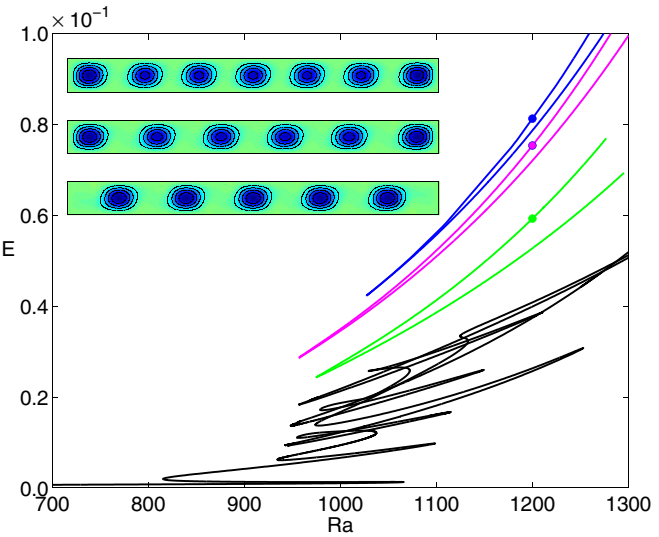

FIG. 11. Mean kinetic energy E for solutions that develop continuously with increasing Rayleigh number Ra from the large-scale flow for $\alpha = 0.05$, showing three additional branches of disconnected states consisting of five (green curve), six (magenta curve), and seven (blue curve) corotating rolls, in addition to the states connected continuously to the LSF (black curve). The insets show the stream function of the steady solutions at the three locations indicated by solid circles, all at Ra = 1200. The parameters are $S = -0.1$, $\tau = 0.01$, $\sigma = 7$, and $\Gamma = 14$.

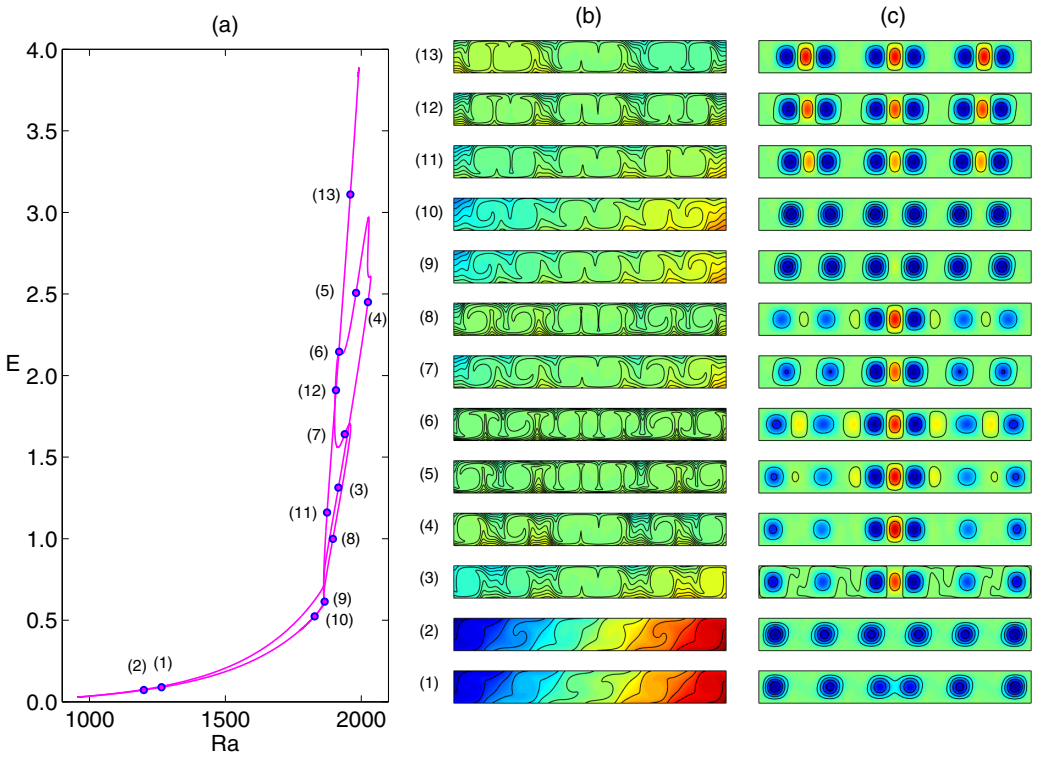

FIG. 12. (a) Complex solution branch obtained by numerical continuation of the steady six-roll state depicted in Fig. 11 when the Rayleigh number Ra is initially decreased, for $\alpha = 0.05$. A transition from corotating rolls back to counterrotating rolls is observed. (b) Concentration C and (c) the contours of the stream function Ψ at the locations indicated in (a). In the concentration contours the same color bar is used for all states. The parameters are $S = -0.1$, $\tau = 0.01$, $\sigma = 7$, and $\Gamma = 14$.

instead take the form of two localized rolls near the lateral walls.

Finally, it is important to notice that the primary Hopf bifurcation of the base flow disappears when α exceeds 0.0473. Figure 10(b) shows the behavior near this value. With increasing α the Hopf bifurcation that destabilizes the lower branch collides with a second Hopf bifurcation, the latter on the upper LSF branch, and the two Hopf bifurcations annihilate in the vicinity of the primary fold at $\alpha \sim 0.0473$, where the two Hopf frequencies coincide. Thus, beyond this critical inclination, the base flow loses stability at the primary fold and remains unstable above it.

A more detailed examination of the R-symmetric solutions that exist near the base flow branch we just discussed reveals the existence of a sequence of disconnected solution curves at larger energy, three of which are shown in Fig. 11. The upper part of the green curve corresponds to states consisting of five equispaced corotating rolls, while the magenta curve corresponds to similar states consisting of six corotating rolls and the blue curve corresponds to states consisting of seven corotating rolls. We illustrate these states in Fig. 11 at the location indicated by the green, magenta, and blue circles. These solutions are numerically stable. In contrast, states consisting of three and four equispaced corotating rolls are connected by the black branch in Fig. 11, as already discussed. The breakup of a snaking structure into a stack of disconnected isolas is a common feature of pattern-forming systems and is seen, for example, in the quadratic-cubic Swift-Hohenberg equation in two spatial dimensions. In this system localized structures in the form of spots initially snake but eventually the snaking breaks up into isolas [35], a consequence of decreasing curvature of the spot as it grows in size. This process resembles that played here by the LSF whose influence is gradually suppressed as Ra increases for fixed inclination α.

In Fig. 12 we show the fate of the six-roll state (magenta curve in Fig. 11) with increasing Ra. The figure is of interest because it shows that the corotating structure does not persist to larger Ra and describes the details of the transition with increasing Ra into a state consisting again of counterrotating rolls resembling those present when $\alpha = 0$. For example, we can distinguish a centered convecton with four single corotating rolls (location 4) and three pulses of convectons (location 8). Similar behavior is obtained when the branch of five-roll states (green curve in Fig. 11) is followed to increasing Ra. The branch of seven corotating roll states (blue curve in Fig. 11) is described below, since, as we will see, it is also reached when a domain-filling state of counterrotating rolls with a counterclockwise central roll is continued to smaller Rayleigh numbers.

In an attempt to look for snaking branches of R-symmetric localized solutions resembling those depicted in Fig. 4 for $\alpha = 0.01$ and in Fig. 7 for $\alpha = 0.03$, we have performed continuation as the Rayleigh number decreases of two equivalent large-amplitude domain-filling states: a state with six pairs of counterrotating rolls plus a counterclockwise central roll and a state with six pairs of counterrotating rolls plus a clockwise central roll. The resulting branches are shown in Figs. 13 and 14.

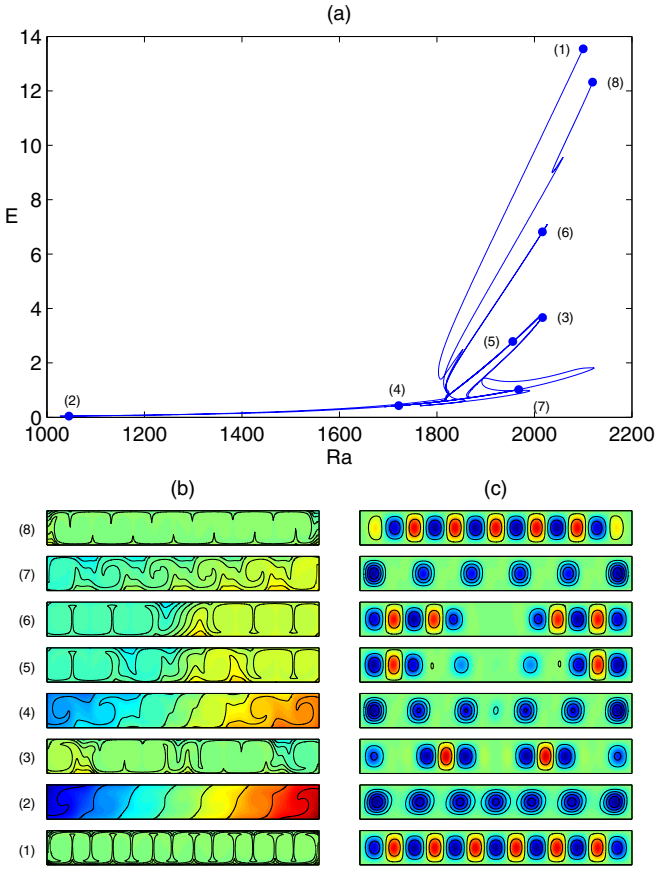

FIG. 13. (a) Complex solution branch obtained by numerical continuation of the steady counterclockwise central roll domain-filling state when the Rayleigh number Ra is initially decreased, for $\alpha = 0.05$. Several transitions from counterrotating rolls to corotating rolls can be observed. (b) Concentration C and (c) the contours of the stream function Ψ at the locations indicated in (a). In the concentration contours the same color bar is used for all states. The parameters are $S = -0.1$, $\tau = 0.01$, $\sigma = 7$, and $\Gamma = 14$.

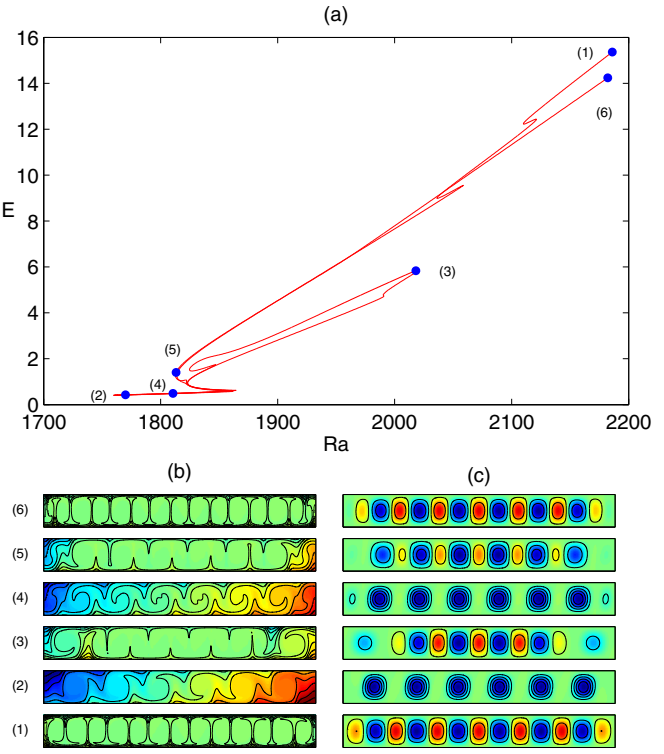

FIG. 14. (a) Complex solution branch obtained by numerical continuation of the steady clockwise central roll domain-filling state when the Rayleigh number Ra is initially decreased, for $\alpha = 0.05$. Several transitions from counterrotating rolls to corotating rolls can be observed. (b) Concentration C and (c) the contours of the stream function Ψ at the locations indicated in (a). In the concentration contours the same color bar is used for all states. The parameters are $S = -0.1$, $\tau = 0.01$, $\sigma = 7$, and $\Gamma = 14$.

In Fig. 13 we summarize the complicated transitions undergone by a domain-filling state with a counterclockwise central roll (solution at location 1). We have identified at least 28 saddle-node bifurcations in the curve we show. Between locations 1 and 2 there is an abrupt weakening of the clockwise rolls with an overall shrinking in width of all clockwise rolls, until only counterclockwise rolls remain (location 2), and the branch of solutions extends to very low values of Ra, Ra $\sim$ 1000. The concentration field undergoes a significant transformation from a perfectly mixed state (location 1) towards a state with a pronounced lateral stratification (location 2), a feature typical of low-amplitude states in inclined systems. This low-amplitude state consists of seven corotating rolls and lies precisely on the blue curve in Fig. 11. Thus the branch in Fig. 13 represents the evolution of the seven-roll state in Fig. 11 to larger values of Ra and E. As the Rayleigh number starts to increase from the lowest value reached, the roll at the center of structure is gradually eliminated and low-amplitude states consisting of six corotating rolls (locations 4 and 7) are visited several times along the path of this curve. Among the high-amplitude states visited by the system, we can highlight a state resembling a two-pulse convecton of counterrotating rolls with two single rolls near the walls (location 3), a state similar to a hole state with two single rolls near the center (location 5), and a pure hole state (location 6). The system finally reaches a new domain-filling state (location 8) in which the central roll is now rotating clockwise. Evidently, the transitions display strong hysteresis, and multiple states consisting of a given number of rolls all exist simultaneously. We expect that these complex transitions are once again a consequence of the no-slip lateral boundary conditions [9].

Figure 14 shows the transitions undergone by the domain-filling state with a clockwise central roll (location 1) when the Rayleigh number decreases. In this case the lowest-Rayleigh-number state reached by the solution branch is around Ra = 1750, so this branch is located to the right of the diagram in Fig. 11. Again the behavior is complicated and 18 saddle-node bifurcations are identified along the branch. As before, the system visits low-amplitude states consisting of six corotating rolls (locations 2 and 4), but only one high-amplitude state resembling a convecton with two single isolated rolls on either side is visited (location 3). In contrast to what happens in Fig. 13, the transitions between the high- and low-amplitude states occur after gradual erosion and subsequent disappearance of the rolls near the lateral walls takes place. The system eventually returns to a domain-filling state but with a slightly

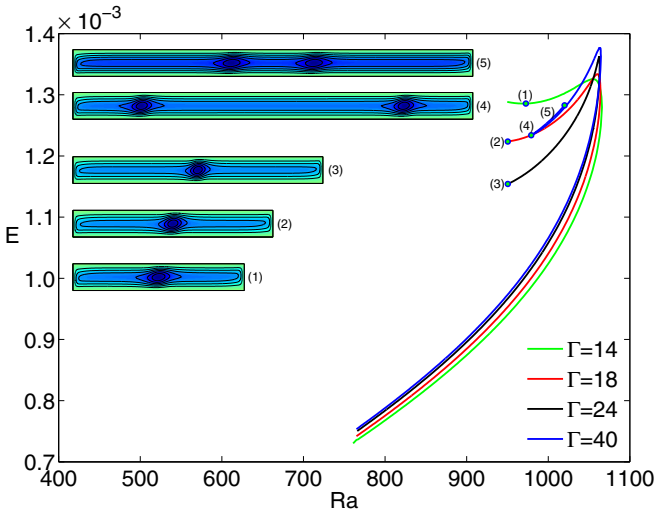

FIG. 15. Mean kinetic energy E for solutions that develop continuously with increasing Rayleigh number Ra from the base flow near the primary fold for four different aspect ratios $\Gamma = 14, 18, 24, 40$. The insets on the left show the stream function at points beyond the fold indicated by open circles. (1) corresponds to $\Gamma = 14$, (2) to $\Gamma = 18$, (3) to $\Gamma = 24$, and (4) and (5) to $\Gamma = 40$. The parameters are $\alpha = 0.05$, $S = -0.1$, $\tau = 0.01$, and $\sigma = 7$.

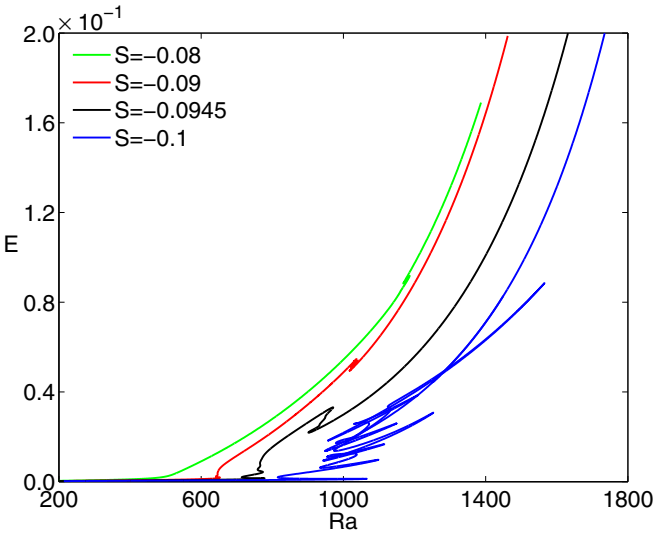

FIG. 16. Mean kinetic energy E for steady solutions obtained by numerical continuation of the large-scale flow with increasing Rayleigh number Ra for four different values of the separation ratio S. The parameters are $\alpha = 0.05$, $\tau = 0.01$, $\sigma = 7$, and $\Gamma = 14$.

different wave number (location 6), in which the central roll is rotating clockwise, as in the initial state (location 1). We emphasize that, despite appearances, the branch in Fig. 14 does *not* represent a continuation of the six-roll state in Fig. 11 to larger Ra and E.

D. Parameter dependence of the base flow branch for $\alpha = 0.05$

We focus now on exploring the sensitivity of the complex $\alpha = 0.05$ base flow branch to the other parameters: aspect ratio Γ, separation ratio S, and Lewis number τ. We analyze first the dependence of the location of the primary fold on the aspect ratio of the domain. This bifurcation arises when the increased energy input can no longer be convected across the whole cell by the large-scale flow and results in the gradual appearance of isolated rolls superposed on the LSF. Figure 15 displays the mean kinetic energy E as a function of Ra for four values of the aspect ratio. In all cases the fold is located at Ra ~ 1050, reflecting the fact that the lateral walls exert negligible influence on its location. In addition, we see that the values of the concentration gradient and the horizontal velocity at the fold are almost independent of the aspect ratio ($\Delta C/\Delta x \sim 0.4$ and $u \sim 0.05$ in nondimensional units). The horizontal velocity and the mean energy of the base flow is fixed by the Rayleigh number and therefore its total energy before the primary fold increases linearly with Γ. For this reason the mean energy is the same and the four curves overlap. After the primary fold, when a single roll emerges, the curves diverge and the higher mean energy curve corresponds to the shorter box. For the longest $\Gamma = 40$ box, two rolls appear near the walls and move towards the center after a further fold bifurcation.

Many of the details of the behavior we have described throughout the paper depend strongly on the precise value of the separation ratio S. Figure 16 shows the solution branches (mean kinetic energy E as a function of the Rayleigh number Ra) for four nearby values of S. The leftmost branch, in green, corresponds to $S = -0.08$. For this value of S the mean kinetic energy of the solution increases monotonically with increasing Rayleigh number; the evolution of the spatial structure of the pattern with Ra is visualized in Fig. 17. We observe that the large-scale flow that forms initially gradually breaks up into cellular patterns as Ra increases. This breakup occurs first near the lateral walls and then invades the interior. This behavior matches exactly the experimental observations reported in [23] for a pure fluid in a slightly inclined cell. The authors observed that one convection roll after another develop stepwise, beginning at the sidewalls and moving towards the middle of the box. This means that the instability does not set in simultaneously in the whole domain, as in the case of horizontal cells, and that an inhomogeneous development of cellular convection takes place instead. We conclude, therefore, that for the σ and τ values used in this paper, the evolution of the large-scale flow with increasing Ra for separation ratios in the range $-0.08 < S < 0$ fits well the phenomenology reported for pure fluids.

For slightly more negative values of S the LSF branch becomes much more complex. Figure 16 shows that already for $S = -0.09$ the solution branch develops a series of folds (red curve) with yet more complex behavior for $S = -0.0945$ (black curve). Figure 18 provides details of the evolution of the solutions in the latter case. This behavior should be compared with that displayed in Fig. 9 for $S = -0.1$ (blue curve in Fig. 16). We see that in all these cases the evolution starts out in a similar manner: The base flow ceases to be featureless and starts to develop a localized roll in the center of the domain. However, the details of the evolution are quite different, even though at various locations the solutions along the branches take the form of four corotating rolls, albeit with different separations, in each case reached by a rather

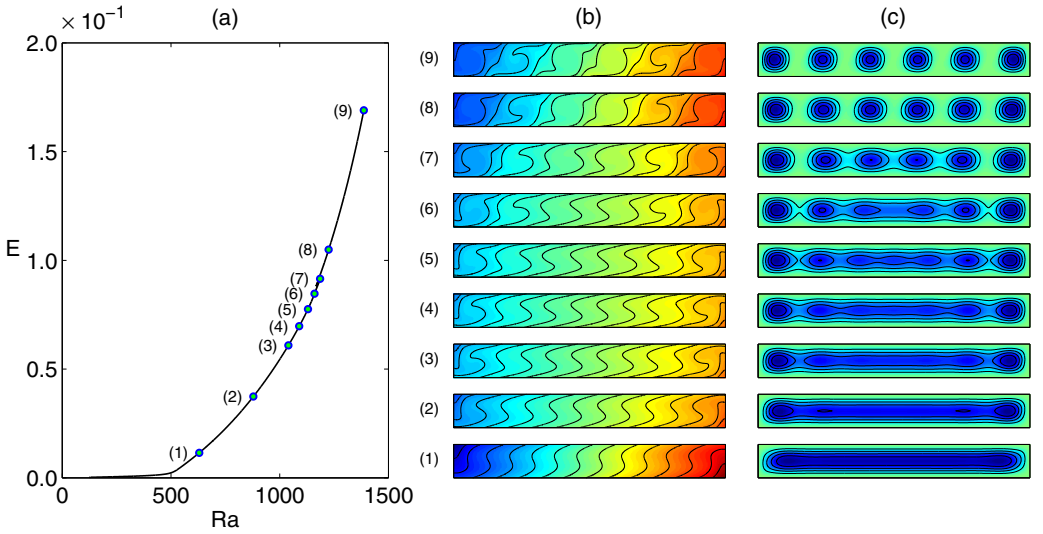

FIG. 17. Detail of the steady solutions obtained by numerical continuation of the base flow with increasing Rayleigh number Ra when $S = -0.08$. (a) Mean kinetic energy E as a function of Ra. (b) Concentration C and (c) the contours of the stream function at the locations indicated in (a). In the concentration contours the same color bar is used for all states. The parameters are $\alpha = 0.05$, $\tau = 0.01$, $\sigma = 7$, and $\Gamma = 14$.

different sequence of transitions. The complexity increases as S becomes more negative.

The precise value of the Lewis number τ also turns out to have a strong influence on the behavior of the LSF branch. Together with the branch already obtained for $\tau = 0.01$, we present in Fig. 19 two additional solution branches for larger values of τ, $\tau = 0.015$ and 0.02. First, we observe that at the largest value of the mean kinetic energy in the figure, the LSF for $\tau = 0.01$ contains three corotating rolls, while that for $\tau = 0.015$ contains only two corotating rolls and that for $\tau = 0.02$ contains only one roll. In addition, the threshold for the disappearance of the quasiparallel flow becomes higher

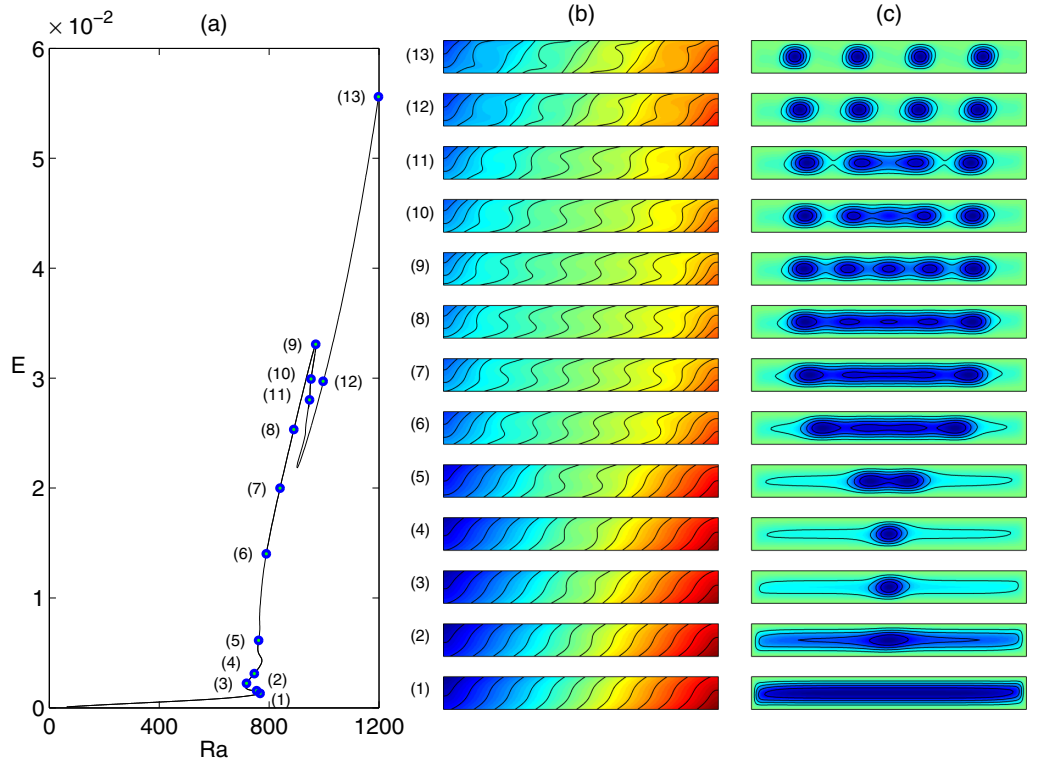

FIG. 18. Detail of the steady solutions obtained by numerical continuation of the base flow with increasing Rayleigh number Ra when $S = -0.0945$. (a) Mean kinetic energy E as a function of Ra. (b) Concentration C and (c) the contours of the stream function at the locations indicated in (a). In the concentration contours the same color bar is used for all states. The parameters are $\alpha = 0.05$, $\tau = 0.01$, $\sigma = 7$, and $\Gamma = 14$.

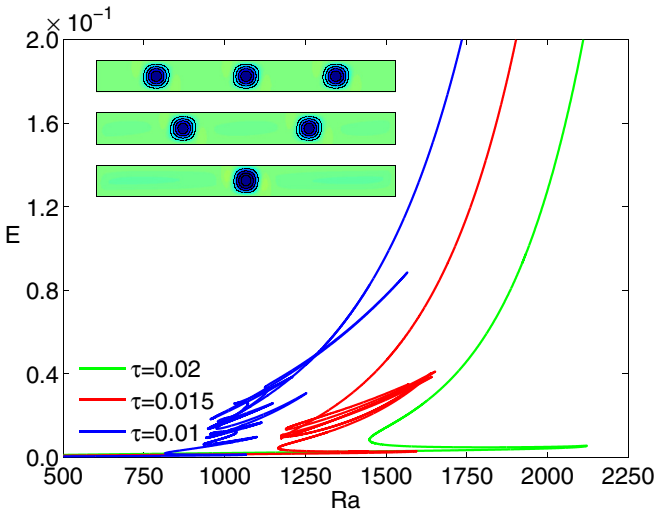

FIG. 19. Mean kinetic energy E for solutions that develop continuously with increasing Rayleigh number Ra from the large-scale flow for different values of the Lewis number τ. From top to bottom, the insets show the stream function of the steady solutions at the upper end of each branch for $\tau = 0.01$, 0.015, and 0.02, respectively. The parameters are $S = -0.1$, $\alpha = 0.05$, $\sigma = 7$, and $\Gamma = 14$.

as τ increases. Indeed, the actual value of the concentration gradient at the lowest turning point has a similar value in the three cases shown and a single roll emerges in the center of the cell in all cases, although at larger amplitudes the number of corotating rolls forming the pattern decreases with increasing τ, as already described. Moreover, the subcritical region between the first two folds grows as the value of τ increases. The complexity of the LSF branch in these cases increases as τ decreases.

IV. CONCLUSION

In this paper we have analyzed numerically the effect of slightly tilting a rectangular cell filled with a negative separation ratio binary mixture. The choice of the physical parameters of the mixture is representative of water-ethanol mixtures ($S = -0.1$, $\tau = 0.01$, and $\sigma = 7$). The study has been done using numerical continuation (with focus on symmetric solutions) and direct numerical simulation. The changes in the bifurcation diagrams that would be expected from the breaking of symmetry that inclination implies are only observed for the smallest inclinations considered in this work, $\alpha = 0.01$ and 0.03. For a slightly larger but still small inclination $\alpha = 0.05$, a completely different scenario is obtained. In addition, the dynamics and patterns arising for $\alpha = 0.05$ depend strongly on the precise values of S and τ.

For $\alpha = 0.01$ and 0.03 the solution branch corresponding to the large-scale base flow that replaces the conduction state in the inclined system extends to large values of Ra without significant change. This base flow undergoes a primary Hopf bifurcation after which chevrons, blinking states, and chaotic blinking states resembling those observed in the absence of inclination may emerge. In contrast, for the slightly larger inclination $\alpha = 0.05$, the behavior of the base flow branch is completely different. The Hopf bifurcations of the large-scale flow no longer exist and the base flow undergoes a fold bifurcation at a low value of Ra and, for $\Gamma = 14$, a single roll appears in the center of the cell. We have referred to the associated fold as the primary fold. When the base flow is numerically continued a variety of small-amplitude states characterized by lateral concentration gradients and made up of corotating rolls that differ in their position and number is encountered. These states are organized in a complex bifurcation diagram that exhibits sharp folds near which splitting, merging, or changing in position of the rolls takes place. We show that, as α increases, the primary fold appears at smaller values of Ra, whereas the primary Hopf bifurcation of the base flow hardly varies with Ra. The primary Hopf bifurcation on the lower part of the LSF branch annihilates with a Hopf bifurcation on the upper part near the primary fold and both disappear when $\alpha \sim 0.0473$. Beyond this inclination, the primary bifurcation of the base flow is the primary fold.

The organization of the large-amplitude localized solutions into snaking branches also undergoes a profound change as the inclination increases. For very small inclinations $\alpha = 0.01$ and 0.03, snaking branches of localized solutions were identified and these coexist with the base flow branch. We showed that the inclination splits the odd-parity snaking branch in the noninclined system into two branches of odd-parity localized solutions, while the even-parity snaking branch breaks up into disconnected branches of asymmetric states. However, for $\alpha = 0.05$, there is no trace of the snaking diagram seen in the noninclined case; we locate its disappearance between $\alpha = 0.03$ and $\alpha = 0.04$. Instead, we now find complex solution branches that visit a great variety of large- and small-amplitude states. The large-amplitude solutions consist of counterrotating rolls and exhibit well-mixed concentration profiles; these include domain-filling states, extended convectons, holes, and multipulse states, the latter either pure or accompanied by single isolated rolls. In contrast, the small-amplitude states consist of corotating rolls with a pronounced lateral stratification. These states do not snake in the sense that the numerous folds that are encountered do not correspond to the usual nucleation of rolls on either side of an existing convecton. Instead, we believe they are ultimately a consequence of the no-slip boundary conditions at the sides, much as occurs in the Swift-Hohenberg equation with mixed (Robin) boundary conditions [36]. However, none of the complex solution branches we computed includes convecton states with a small number of counterrotating pairs of rolls. If such convectons exist, they have to be located on distinct solution branches. These could conceivably be located by two-parameter continuation focusing on the precise way in which the snaking branches disappear, but such a study is beyond the scope of the present work, since it would require exhaustive computations for many different values of α.

Although the primary fold on the LSF branch and the right fold at high values of the Rayleigh number on the lower part of the snaking branches both appear to move off to $\mathrm{Ra} = \infty$ as α decreases to zero, they do not appear to be related. As an example, for $\alpha = 0.03$ the lower part of the counterclockwise central roll snaking branch turns around in a fold at $\mathrm{Ra} \sim 9300$ while the LSF branch turns around in a different fold (the primary fold) located at $\mathrm{Ra} \sim 44\,000$. There is no connection between the branches when continued beyond these folds.

We have also analyzed the influence of varying the aspect ratio Γ of the cell, the separation ratio S, and the Lewis number τ on the base flow branch obtained for $\alpha = 0.05$. The location of the primary fold is not affected by Γ, but the number of corotating rolls that appear after the primary fold increases to 2 for $\Gamma = 40$. In contrast, the precise value of S and τ alters dramatically the behavior of the base flow branch. In fact, our initial choice of the parameters of the mixture, $S = -0.1$ and $\tau = 0.01$, is located in a region of parameter space in which the behavior is particularly complex. As S increases, a transition to a smoother branch takes place along which the large-scale flow that forms initially gradually breaks up into a cellular pattern as Ra increases. This breakup occurs initially near the lateral walls and then invades the interior, much as occurs in inclined pure fluid convection [23]. As τ increases, the location of the primary fold moves to higher values of Ra and the region of existence of the base flow increases. Moreover, the additional folds on the LSF branch present for smaller τ progressively disappear.

To sum up, we have shown that a slight tilt of a rectangular cell filled with a negative separation ratio binary mixture changes the behavior of the system in several ways. On the one hand, the complex spatiotemporal dynamics resulting from the Hopf bifurcation of the base flow disappears at a certain inclination when the Hopf bifurcation passes the primary fold. On the other hand, the inclination gives rise to a rich diversity of small-amplitude localized corotating-roll states with significant lateral concentration gradients and to larger-amplitude localized solutions that are organized in complicated snaking diagrams that cover a broad range of Rayleigh numbers. Of particular significance is the fact that the arrangement of the localized solutions into snaking branches is completely destroyed already at very small inclinations. In noninclined binary convection the snaking structure persists after changes in the lateral boundary conditions [8,9] or in the top and bottom boundary conditions [30]. However, it is evidently not robust with respect to the introduction of a slight inclination into the system. Another example in which the snaking diagram does not persist is discussed in recent work of Lo Jacono *et al.* [37]. In this system, natural doubly diffusive convection in a vertical slot, changing the boundary condition at one of the vertical walls to a Robin or mixed concentration boundary condition, suffices to destroy the snaking diagram: All localized states of the snaking diagram now travel and may connect with separate branches of traveling pulses.

We have presented numerical evidence that a very small inclination produces significant changes in the dynamics of binary fluid convection. In fact, this should not come as a complete surprise. As originally shown by Wunsch [38] and Phillips [39], a stratifying agent in contact with an inclined no-flux boundary condition necessarily leads to a diffusion-driven flow upward along the lower boundary and downward along the upper boundary. The physics behind this observation is simple: Isopycnals cannot be horizontal near inclined boundaries and still satisfy the no-flux boundary condition. The dependence of the resulting flow on the inclination angle α is explored experimentally in Ref. [40]. When the separation ratio S is sufficiently negative the present system resembles that studied by Wunsch and Phillips: A small applied temperature difference generates a stable stratification subject to an effective no mass-flux boundary condition. Thus a large-scale flow is present even for very small Rayleigh numbers (cf. Fig. 16) and it is this flow that evolves into many of the structures exhibited in this paper when the imposed temperature difference, i.e., the Rayleigh number Ra, increases and the diffusively generated flow starts competing with destabilizing thermal buoyancy effects. Despite the complexity in the resulting behavior described here, the study of the slightly inclined system is far from complete. On the one hand, in the two-dimensional system, computation of the branches of asymmetric steady solutions, exploration of new regions of parameter space, or a study of stable spatiotemporal dynamics are some aspects that deserve future attention. Three-dimensional simulations would also be of interest but are much more costly. However, provided the transverse direction is small enough, we expect that the basic physics of the problem will persist in three dimensions, as happens in pure fluids with the onset of corotating rolls, although the increase in dissipation arising from the additional walls is expected to postpone the various transitions to larger values of the Rayleigh number. On the other hand, while some experiments dealing with tilted vertically elongated cells filled with a binary mixture are available due to their application to thermogravitational columns, we are not aware of any systematic experimental study of the slightly inclined horizontally elongated case. Our calculations indicate that this system would benefit from such experiments because of the interesting physics that it entails.

ACKNOWLEDGMENTS

This work was supported in part by the Spanish Ministry of Science, Innovation and Universities (MICINN) under Grant No. FIS2017-85794-P (I.M., O.B., and A.A.) and the National Science Foundation (USA) under Grant No. DMS-1613132 to the University of California, Berkeley (E.K.).

[1] J. Fineberg, E. Moses, and V. Steinberg, Phys. Rev. Lett. **61**, 838 (1988).
[2] V. Steinberg, J. Fineberg, E. Moses, and I. Rehberg, Physica D **37**, 359 (1989).
[3] P. Kolodner, C. M. Surko, and H. Williams, Physica D **37**, 319 (1989).
[4] P. Kolodner, Phys. Rev. E **47**, 1038 (1993).
[5] O. Batiste, I. Mercader, M. Net, and E. Knobloch, Phys. Rev. E **59**, 6730 (1999).
[6] O. Batiste, E. Knobloch, I. Mercader, and M. Net, Phys. Rev. E **65**, 016303 (2001).
[7] I. Mercader, O. Batiste, A. Alonso, and E. Knobloch, Phys. Rev. E **80**, 025201(R) (2009).
[8] I. Mercader, O. Batiste, A. Alonso, and E. Knobloch, Fluid Dyn. Res. **42**, 025505 (2010).
[9] I. Mercader, O. Batiste, A. Alonso, and E. Knobloch, J. Fluid Mech. **667**, 586 (2011).
[10] E. Knobloch and D. R. Moore, Phys. Rev. A **37**, 860 (1988).

[11] V. Steinberg and E. Kaplan, in *Spontaneous Formation of Space-Time Structures and Criticality*, edited by T. Riste and D. Sherrington, NATO Advanced Studies Institute, Series B: Physics (Plenum, New York, 1991), pp. 207–244.
[12] O. Batiste, E. Knobloch, A. Alonso, and I. Mercader, J. Fluid Mech. **560**, 149 (2006).
[13] E. Bodenschatz, W. Pesch, and G. Ahlers, Annu. Rev. Fluid Mech. **32**, 709 (2000).
[14] K. E. Daniels, B. B. Plapp, and E. Bodenschatz, Phys Rev. Lett. **84**, 5320 (2000).
[15] K. E. Daniels, O. Brausch, W. Pesch, and E. Bodenschatz, J. Fluid Mech. **597**, 261 (2008).
[16] P. Subramanian, O. Brausch, K. E. Daniels, E. Bodenschatz, T. M. Schneider, and W. Pesch, J. Fluid Mech. **794**, 719 (2016).
[17] J. F. Torres, D. Henry, A. Komiya, and S. Maruyama, J. Fluid Mech. **756**, 650 (2014).
[18] O. Shishkina and S. Horn, J. Fluid Mech. **790**, R3 (2016).
[19] M. Ouriemi, P. Vasseur, and A. Bahloul, Numer. Heat Transfer A **48**, 547 (2005).
[20] A. Zebib and M. M. Bou-Ali, Phys. Rev. E **79**, 056305 (2009).
[21] F. Croccolo, F. Scheffold, and A. Vailati, Phys. Rev. Lett. **111**, 014502 (2013).
[22] A. Alonso, I. Mercader, and O. Batiste, Phys. Rev. E **97**, 023108 (2018).
[23] K. R. Kirchartz and H. Oertel, J. Fluid Mech. **192**, 249 (1988).
[24] I. Mercader, O. Batiste, and A. Alonso, Int. J. Numer. Meth. Fluids **52**, 707 (2006).
[25] S. Hugues and A. Randriamampianina, Int. J. Numer. Meth. Fluids **28**, 501 (1998).
[26] S. Zaho and M. J. Yedlin, J. Comput. Phys. **113**, 215 (1995).
[27] C. K. Mamun and L. S. Tuckerman, Phys. Fluids **7**, 80 (1995).
[28] V. Frayssé, L. Giraud, S. Gratton, and J. Langou, Public domain software and matrix collection, CERFACS Report No. TR/PA/03/3, CERFACS, available at www.cerfacs/algor/Softs (2003).
[29] C. Martel and J. M. Vega, Nonlinearity **11**, 105 (1998).
[30] I. Mercader, O. Batiste, A. Alonso, and E. Knobloch, J. Fluid Mech. **722**, 240 (2013).
[31] S. M. Houghton and E. Knobloch, Phys. Rev. E **84**, 016204 (2011).
[32] D. Avitabile, M. Desroches, E. Knobloch, and M. Krupa, Proc. R. Soc. London A **473**, 20170018 (2017).
[33] R. C. Paliwal and C. F. Chen, J. Fluid Mech. **98**, 755 (1980).
[34] C. F. Chen and S. Thangam, J. Fluid Mech. **161**, 161 (1985).
[35] S. McCalla and B. Sandstede, Physica D **239**, 1581 (2010).
[36] S. M. Houghton and E. Knobloch, Phys. Rev. E **80**, 026210 (2009).
[37] D. Lo Jacono, A. Bergeon, and E. Knobloch, Phys. Rev. Fluids **2**, 093501 (2017).
[38] C. Wunsch, Deep-Sea Res. **17**, 293 (1970).
[39] O. M. Phillips, Deep-Sea Res. **17**, 435 (1970).
[40] T. Peacock, R. Stocker, and J. M. Aristoff, Phys. Fluids **16**, 3503 (2004).